

Relationships between the mode II fracture toughness and microstructure of thermal spray coatings

P.J. Callus^{a,*}, C.C. Berndt^b

^a Department of Materials Engineering, Monash University, Clayton, Victoria 3168, Australia

^b Thermal Spray Laboratory, Department of Materials, Science and Engineering, State University of New York at Stony Brook, New York, NY 11794-2275, USA

Received 19 October 1998; accepted 11 January 1999

Abstract

A novel test specimen geometry was used to determine the critical mode II strain energy release rate, G_{IIc} , of nine batches of air- and low-pressure plasma-sprayed coatings. These data will supplement those from existing mode I fracture toughness tests and serve as a basis for understanding the more complex mixed mode loading conditions experienced by operational coatings. It is proposed that coating toughness is dominated by microporosity, macroporosity, unmelted particles, and microcracks parallel and perpendicular to the coating surface. The concept of Quality Indices was introduced, where each batch of coatings was ranked according to the prevalence and severity of these microstructural defects. The Quality Indices, G_{IIc} and failure morphology were plotted on a failure map. This showed that an improved coating microstructure, as indicated by rising Quality Indices, was associated with an increasing G_{IIc} and a change in failure morphology. © 1999 Published by Elsevier Science S.A. All rights reserved.

Keywords: Defects; Fracture toughness test; Interfaces; Scanning electron microscopy

1. Introduction

Significant improvements in deposition equipment over the last 40 years have produced corresponding advances in the quality and reliability of thermal spray coatings. However, as deposition technology matures, alternative routes must be sought if the rate of improvement is to continue. One promising route is through an understanding of the role of microstructure in coating failure.

Thermal spray coatings fail as a result of the propagation and link-up of microcracks. Therefore, fracture toughness testing holds the greatest potential for characterizing their mechanical behaviour. It is the microstructure that links the deposition parameters to coating toughness, which in turn dictates service performance. Through an understanding of these relations, the deposition conditions may be controlled to enhance features

that are beneficial to coating performance and suppress those that lead to failure.

In this work, the mode II fracture toughness of four typical thermal spray coatings, NiAl, duplex NiAl+Al₂O₃, duplex NiAl+ZrO₂-8 wt% Y₂O₃ (YSZ), and 45 wt% Ti-55 wt% Ni (TiNi), were determined using a novel test specimen. In addition, the prevalence and severity of the microstructural features expected to influence coating properties were quantified using the concept of Quality Indices. Finally, the relation between microstructure, toughness and failure morphology was presented on a failure map.

1.1. Important microstructure features

1.1.1. Lamellae

Thermal spray devices impart thermal and kinetic energy into the coating feedstock, producing molten droplets that are accelerated towards the substrate. Upon impact with the substrate, the material within the droplets flows outward to produce pancake-shaped discs. The solidified discs are typically 3–10 μm thick and 50–150 μm in diameter, known as lamella, and

* Corresponding author. Present address: Department of Defence, Aeronautical and Maritime Research Laboratory, PO Box 4331, Melbourne, Victoria, Australia. Tel.: +61 396267053; fax: +61 396267174.
E-mail address: paul.callus@dsto.defence.gov.au (P.J. Callus)

constitute the basic structural unit of thermal spray coating.

1.1.2. Porosity

Porosity strongly influences the mechanical properties of thermal spray coatings, with properties decreasing as porosity increases [1–3]. Coatings contain a bimodal pore distribution, with one peak between 10 and 30 μm called macroporosity, and a second much finer peak around 0.1 μm called microporosity [4]. Macroporosity refers to the voids between lamellae, where spreading droplets are too viscous to fill surface irregularities, and is commonly referred to as coating porosity. In contrast, microporosity is caused by the incomplete wetting of the existing coating surface by the freshly impacted and spreading droplets. The extent of wetting depends on both the thermodynamics of the impact event and the deposition parameters, and so is difficult to control using spraying conditions alone. The orientation, size and large number of micropores suggest that such defects are one of the most important factors influencing the mechanical properties of thermal spray coatings.

With a typical 1 cm x 1 cm x 500 μm volume of coating, there are in the order of 10^5 – 10^7 lamellae and, if it is assumed that some part of the surface of each lamellae is separated from its neighbour, a similar number of micropores. In addition, the tips of these micropores are atomically sharp. Clearly, these micropores represent a significant stress concentration.

Between 20 and 50% of the projected area between any two adjacent lamellae is in true intimate contact [4], the remaining interfacial regions being separated by 0.1 μm -thick micropores. With some variations, lamellae conform to the topography of the previously coated material. Thus, while the lamellae surfaces and, therefore, the orientation of micropores are reasonably tortuous and may even exceed 90° relative to the plane of the coating, in general, they are within 30° or so of this plane. It has been conjectured that the through-thickness elastic modulus of thermal spray coatings is proportional to the area fraction of intimate interlamellar contact [5]. The moduli of sintered and atmospheric plasma-sprayed (APS) ZrO_2 have been reported as 200 and 48 GPa, respectively. This implies an intimate contact area of 25%, in agreement with Ref. [4]. Further support for this argument was given in Ref. [6], where porosity was modelled as ellipsoids with zero stiffness. The modulus of APS Al_2O_3 was accurately predicted if the aspect ratio of these pores was assumed to be 1:100. In this case 0.1- μm -thick pores would be 10 μm long. Again, this is consistent with previous observations of coating microstructure [4].

1.1.3. Microcracking

1.1.3.1. Cracking through individual lamellae The lamellae within thermal sprayed ceramic coatings are

generally cracked. The process of crack formation begins immediately after the molten droplet impacts the surface. As material within the droplet flows outward, bonds are formed with the surface on which the droplet has been deposited. The droplet then solidifies and shrinks, while at the same time, the surface onto which it impacts remains largely unchanged. Although the combined action of the incoming hot coating material and continued passage of the thermal spray torch may raise substrate temperatures up to 600°C, the contraction of lamellae is generally far greater than the expansion of the substrate. This results in residual strains within the lamellae. When these strains exceed the strain-to-failure of the coating material, they will be relieved through the generation of through-thickness cracks in the lamellae. However, this cracking only relieves the peak stresses; it is usual for significant strain energy to remain in the coating as a residual deposition stress [7].

1.1.3.2. Cracking in the coating perpendicular to the substrate

The mechanism for the formation of cracks through the thickness of the coating is identical to that for cracks through individual lamellae but is transformed to the scale of the coating. If contraction of the coating exceeds that of the substrate, then cracks may propagate in the through-thickness direction. Such features are termed segmentation, or mud-flat, cracks and, although they expose the substrate at the root of these cracks, they do not severely degrade coating performance. They leave free-standing islands of coating material, which adhere to the substrate, but not to adjacent islands. This substantially increases the strain tolerance of coatings because the islands are free to expand and contract, with little lateral restraint [8–10].

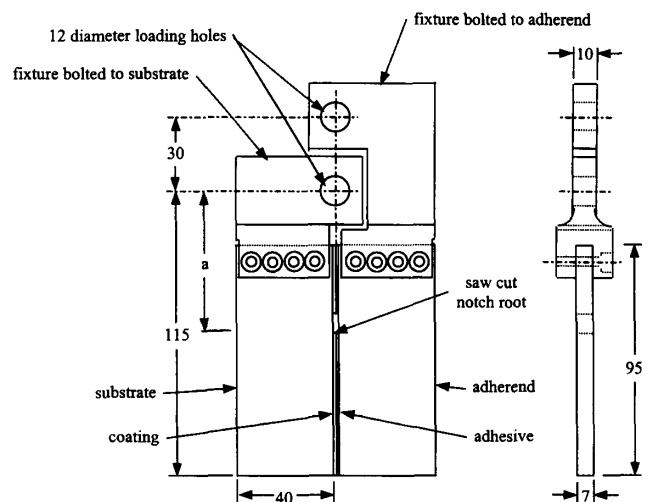


Fig. 1. Mode II test specimen and attached loading fixtures. All dimensions are in millimetres.

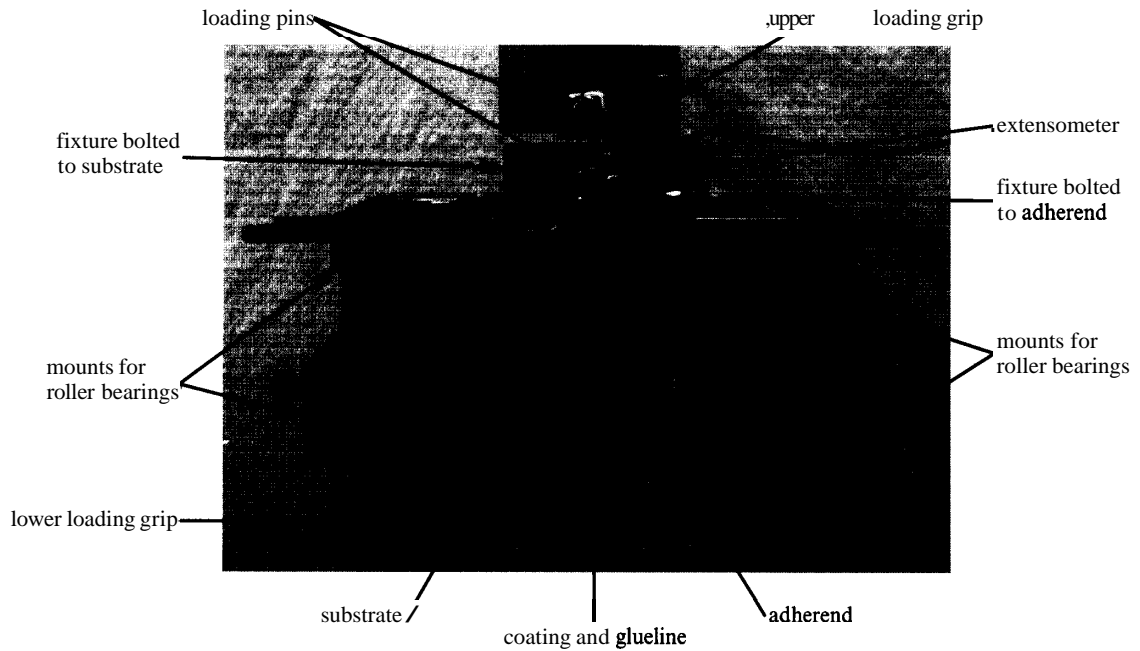


Fig. 2. Configuration used for the mode II tests.

1.1.3.3. Cracking in the coating parallel to the substrate Microcracking parallel to the coating surface greatly reduces life span since, under load, these cracks propagate to produce delamination and spalling. This directly exposes the substrate, or reduces the coating thickness, over an area much larger than an equivalent area of cracking oriented perpendicular to the plane of the coating. The parallel microcrack morphology results from shear stresses generated at the interface between freshly impacted lamellae and the previously deposited surface. This shear stress is at a maximum at free edges, such as the periphery of individual lamellae, and stress concentrators such as segmentation cracks, unmelted particles, microporosity and interlamellar oxides.

1.1.4. Interlamellar oxide interfaces

Droplets of metallic and non-oxide ceramic materials react with atmospheric oxygen during their flight to the substrate. The resultant oxide layer around each lamella

reduces the area fraction of intimate contact. The thickness of these oxide layers, and their consequent effect on mechanical properties, may be minimized by optimizing the spraying conditions. The highest-quality thermal spray coatings are produced using techniques such as low-pressure plasma spraying (LPPS), where oxygen is completely excluded from the molten droplets and hot coating surface during deposition.

1.1.5. Unmelted powder

In most spraying processes, at least some of the coating material will not be fully molten when it impacts the substrate. These particles have either not melted, or have melted and cooled prior to impact. Such particles do not spread or flatten into lamellae and possess a very small area of intimate contact with adjacent material. In order to maximize coating integrity, it is important to minimize the number of unmelted particles in coatings.

Table 1
Priorities for the determination of Cross-sectional and Surface Quality Indices

| Priority | Selection criteria for Cross-sectional Quality Indices | |
|----------|--|---|
| 1 | Microcracks parallel to coating | Index decreased as number and extent increased |
| 2 | Specific number of unmelted particles | Index decreased as number increased |
| 3 | Macroporosity | Index decreased as porosity increased |
| 4 | Microcracks perpendicular to coating | Index decreased as number and extent increased |
| | Selection criteria for Surface Quality Indices | |
| 1 | Extent of lamellae melting | Index decreased as extent of melting decreased |
| 2 | Relative area of smooth surface | Index decreased as fraction of well melted lamellae decreased |
| 3 | Fine microcracks through lamellae | Index decreased as number of microcracks decreased |

Table 2
Cross-sectional Quality Indices and coating descriptions for the batches

| Index | Batch | Material | Description |
|-------|-------|-------------------------------------|--|
| 9 | 9 | TiNi | High aspect ratio lamellae with no visible interlamellar interfaces or macroporosity. A number of larger unmelted particles |
| 8 | 1 | NiAl | High aspect ratio lamellae. Oxide film around lamellae is very thin and discontinuous. Few unmelted particles. Little porosity. Few oxide inclusions |
| 7 | 3 | NiAl–Al ₂ O ₃ | Second highest macroporosity in terms of pore size and total pore volume. Pores distributed uniformly through the coating. No microcracking |
| 6 | 6 | NiAl–Al ₂ O ₃ | Pore size and content was lower than in batch 3, but there were a number of vertical microcracks that penetrated to the bond cast-ceramic interface |
| 5 | 2 | NiAl | The number of partially melted particles and the thickness of interlamellar oxide interfaces were larger than the other NiAl coating |
| 4 | 5 | NiAl–Al ₂ O ₃ | The largest pore size and highest content of microporosity of all coatings, although there was no cracking parallel to the substrate–coating interface |
| 3 | 4 | NiAl–Al ₂ O ₃ | A distinct crack, parallel to the plane of the coating, 200 μm from the substrate and a less obvious discontinuity 400 μm into the coating |
| 2 | 7 | NiAl–YSZ | Coatings contained distinct parallel microcracks 200 μm from the bond coat. Perpendicular microcracks were observed with a separation of 200–1000 μm |
| 1 | 8 | NiAl–YSZ | The parallel and perpendicular microcracks were wider, and the perpendicular microcracks more closely spaced, than those in batch 7 |

1.1.6. Phase structure

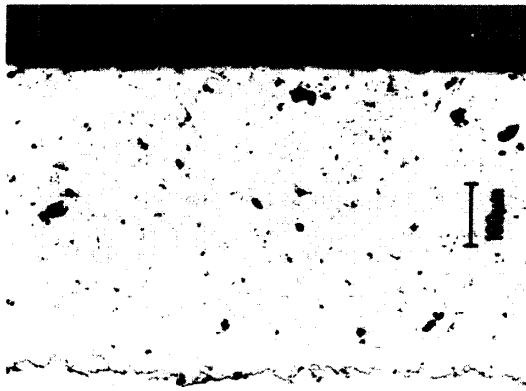
The temperature difference between impacting droplets and substrates results in severe thermal quenching of lamellae, with cooling rates reaching 10^7 K s^{-1} [11]. These produce non-equilibrium phases, for example bulk Al₂O₃ is composed of the α phase, whereas sprayed coatings are almost exclusively the metastable γ phase [11]. Knowledge of the non-equilibrium phases that are formed, and the properties of these phases, is required for the prediction of coating properties. It is proposed that the phase structure of the lamellae is only a secondary factor, with microstructural defects such as microporosity and microcracks dominating the mechanical properties of thermal spray coatings.

1.2. Stresses

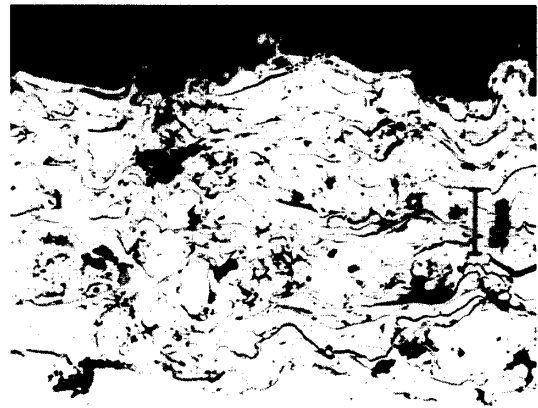
Service stresses, such as those generated by elevated temperature, thermal cycling, oxidation, corrosion or mechanical loading of the coating or substrate, add to the residual deposition stresses. Significant work has been directed at determining the type and magnitude of both sources of stress. These analyses show tremendous variations, ranging from the entire coating being subjected to compressive loads large enough to buckle and spall the coating [9], through mixed tensile/compressive loads [12], to the entire coating being subjected to tensile loads, which lead to segmentation cracks [13]. The precise stress distribution is critically dependent on

Table 3
Surface Quality Indices and coating descriptions for the batches

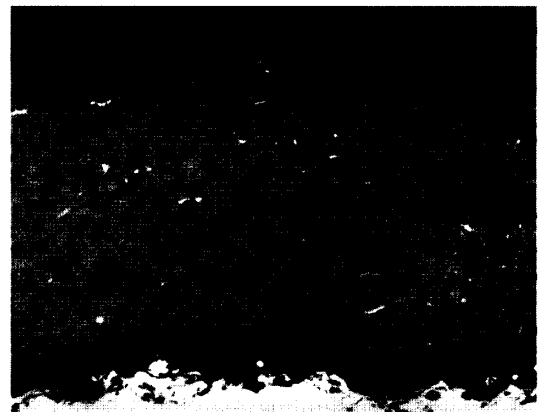
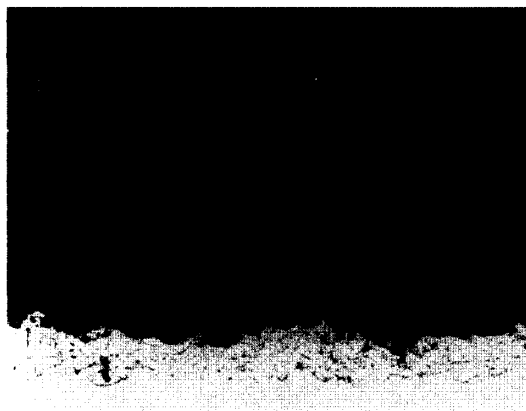
| Index | Batch | Material | Description |
|-------|-------|-------------------------------------|---|
| 9 | 1 | NiAl | The centre of most lamellae were well melted. Significant quantities of incompletely melted material remained at the edges of, and between adjacent, lamellae |
| 8 | 2 | NiAl | Similar appearance to batch 1, with less melting within lamellae and a greater proportion of unmelted material between lamellae |
| 7 | 6 | NiAl Al ₂ O ₃ | A reasonable level of particle melting with minor quantities of fine unmelted particles |
| 6 | 9 | TiNi | Most material appears softened rather than fully melted. These soft particles had maintained their shape upon impact rather than flattening into lamellae |
| 5 | 4 | NiAl Al ₂ O ₃ | Extent of melting in a few lamellae appears greater than for batch 9, but the fraction of fine unmelted particles had increased |
| 4 | 7 | NiAl–YSZ | Extent of lamellae melting lower than batch 4. Larger microcracks that were observed in the cross-sections were also identified |
| 3 | 8 | NiAl–YSZ | Although the core of the lamellae were still relatively well melted, the fraction of undeformed material around the edges had increased from batch 7 |
| 2 | 5 | NiAl–Al ₂ O ₃ | Regions of most lamellae were well melted, but almost all of these contained unmelted material. Fine unmelted particles over 40% of coating |
| 1 | 3 | NiAl–Al ₂ O ₃ | Similar to batch 5, except that the unmelted particles appeared more angular, indicating that they had not even softened in the plasma plume |



Batch 9, TiNi, Index 9



Batch 1, NiAl, Index 8

Batch 3, NiAl-Al₂O₃, Index 7Batch 6, NiAl-Al₂O₃, Index 6

Batch 2, NiAl, Index 5

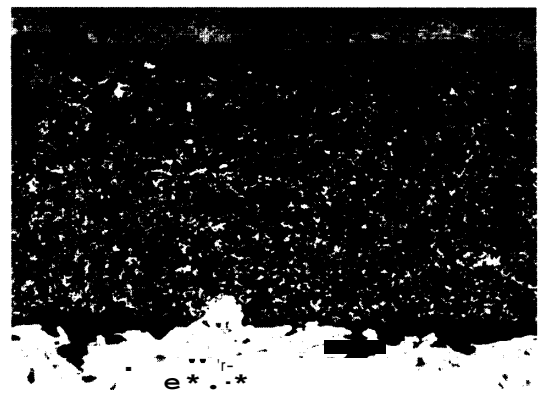
Batch 5, NiAl-Al₂O₃, Index 4

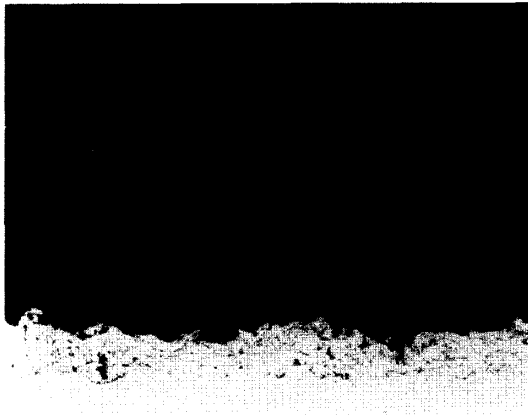
Fig. 3. Cross-section of as-sprayed coatings indicating batch number, coating material and Cross-sectional Indices.

many parameters, including the effective coefficient of thermal expansion of the coating and substrate, local temperatures, the volume of any embedded reaction or corrosion products, and the coating microstructure, particularly the finely dispersed laminar microporosity. It is probable that coatings are subjected to stress both transverse to the plane of the coating and biaxially within the plane of the coating [14]. In many situations,

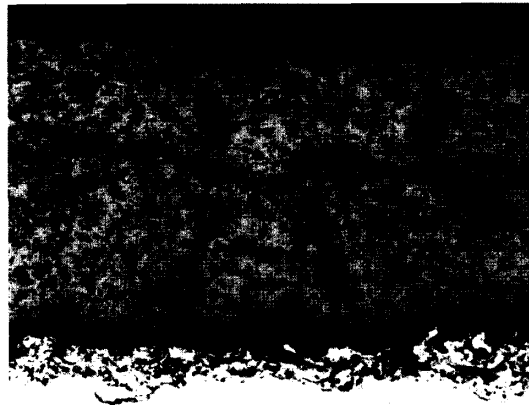
such as near coating edges or under transient mechanical contact or thermal loads, significant shear stresses parallel to the plane of the coating will also be present [15].

1.3. Mechanical testing

An increasing number of fracture toughness tests are being developed for thermal spray coatings [16–19], the

Batch 4, NiAl-Al₂O₃, Index 3

Batch 7, NiAl-YSZ, Index 2



Batch 8, NiAl-YSZ, Index 1

Fig. 3. (continued)

majority of which are designed to induce mode I fracture. Although the data from these tests have proven useful, there exists a need to develop tests that more closely simulate the loading conditions experienced by operational coatings.

Operational coatings are subjected to mixed mode I and mode II loading. The aim of testing should therefore be to determine the entire mode I/mode II envelope. In this work, it was decided that, although there are still areas of mode I behaviour that are not well understood, the behaviour of coatings subjected to mode II loading would be evaluated. Apart from the previous work of the authors [20–22], no attempts have made to measure the mode II fracture toughness of thermal spray coatings. The elucidation of the more complex mixed mode behaviour will remain the subject of future research.

2. Experimental

2.1. Mode II fracture toughness test

2.1.1. Coating deposition

The critical mode II strain energy release rate, G_{IIc} , of coatings was measured using the novel test geometry

shown in Fig. 1 [22]. Substrates and adherends were constructed from mild steel bar, with the mating 95 mm x 7 mm faces of each substrate and adherend pair ground flat. The ground edges of substrates were cleaned with acetone, grit-blasted and a coating deposited. Twelve specimens were prepared in each batch, with all coatings deposited in the same run.

The compositions of the nine batches were as follows: (1) batches 1 and 2, APS NiAl (Metco 450NS), (2) batches 3–6, duplex APS NiAl (Metco 450NS)+Al₂O₃ (Metco 101), (3) batches 7 and 8, duplex APS NiAl (Metco 450NS)+YSZ (Metco 240NS), and (4) batch 9, LPPS TiNi (powder manufactured by the Guangzhou Research Institute for Non-Ferrous Metals). The deposition conditions used for these coating were those recommended by the powder manufacturers and are reported elsewhere [25].

2.1.2. Specimen construction

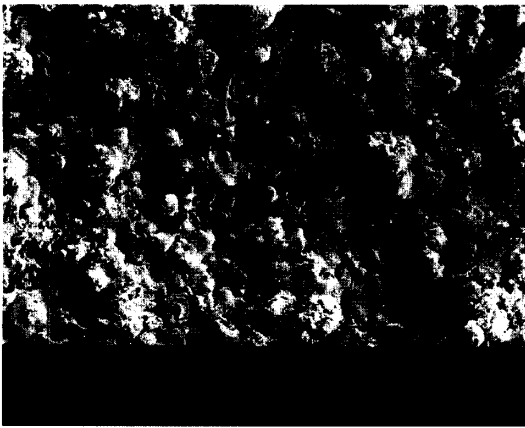
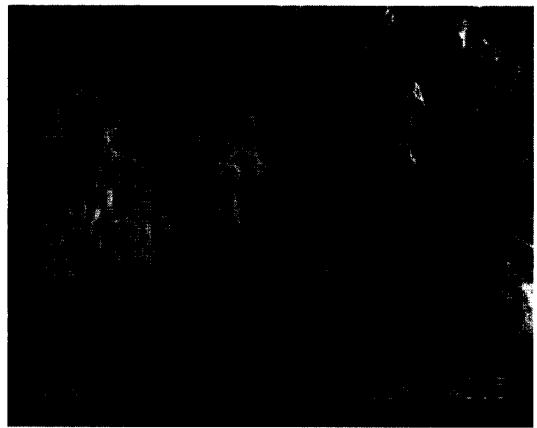
Holes were drilled in the substrate and adherend after spraying to facilitate the attachment of the loading fixtures. An artificial crack tip was made, since the coatings had been deposited along the entire length of



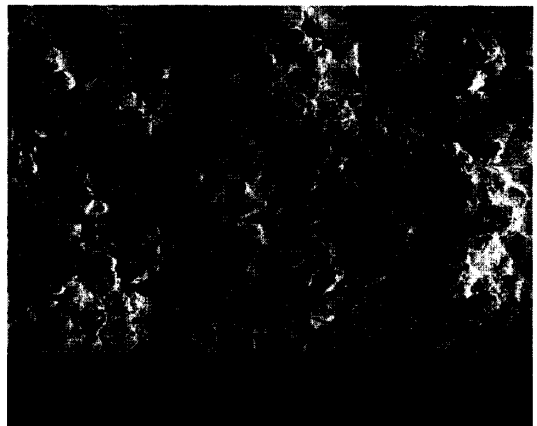
Batch 1, NiAl, Index 9



Batch 2, NiAl, Index 8

Batch 6, NiAl-Al₂O₃, Index 7

Batch 9, TiNi, Index 6

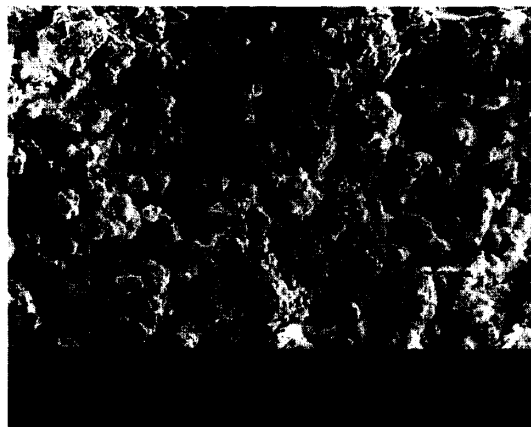
Batch 4, NiAl-Al₂O₃, Index 5

Batch 7, NiAl-YSZ, Index 4

Fig. 4. As-sprayed coating surfaces indicating batch number, coating material and Surface Quality Indices.

the substrate, by cutting through the coating using a hack saw. The substrate were clamped in a rigid fixture and a strip of FM 73M epoxy film adhesive (American Cyanamid Company), cut to the shape of the region to be tested, lightly pressed against the coating. The adherend was then pressed against the adhesive and clamped in the fixture. A 0.1-mm-thick strip of Teflon was positioned between the coating and adherend, at the

opposite end of the specimen to that being bonded, before the clamp was tightened. This maintained specimen alignment during curving by preventing the notch faces from being pressed together. The FM 73M was cured by heating to 120°C for 1 h. Specimens were then removed from the clamping fixture and the **glueline** smoothed with emery paper. All adhesive was removed from the notch root using a jewellers' saw, with cutting



Batch 8, NiAl-YSZ, Index 3

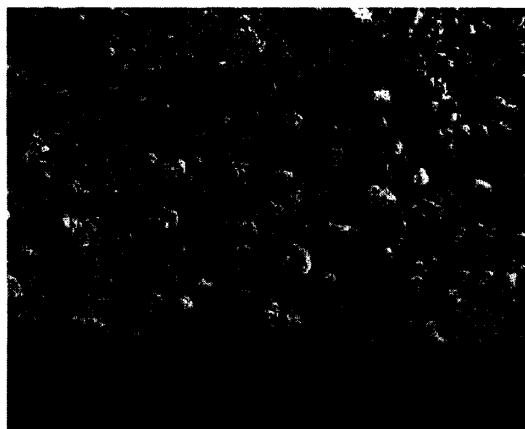
Batch 5, NiAl-Al₂O₃, Index 2Batch 3, NiAl-Al₂O₃, Index 1

Fig. 4. (continued)

continued until fresh coating was exposed at the notch root. The Teflon strip was cut out using a razor blade. Finally, the loading fixtures were bolted to the substrate and adherend.

2.1.3. Test procedure

The completed specimens were mounted in loading grips and aligned with the loading axis. Alignment was achieved by adjusting the position of mounts in which the lower loading pin was located. Mounts for radial ball bearings were then positioned at each corner of the specimen. The bearings were adjusted to press lightly against the sides of the substrate and adherend, preventing mode I opening of the two specimen halves. An extensometer was located on the loading pins to record displacements during the test. The final test configuration is shown in Fig. 2. Tests were conducted by raising the ram at 0.72 mm min^{-1} until the coating failed.

2.1.4. Calculation of fracture toughness

The critical mode II strain energy release rate, G_{IIc} , of the coatings was determined using the compliance calibration technique [23]. Specimen compliance was

calculated using the displacements measured by the extensometer. At the completion of testing, the compliances for all specimens of each material were plotted as a function of the non-dimensional crack length, a/W , which was measured before the test. A least-squares linear fit was made through these data, and the resulting compliance calibration, $dC/d(a/W)$, used to solve Eq. (1). The other terms in Eq. (1) are the failure load, P_c , specimen thickness, $B=7 \text{ mm}$, and specimen width, $W=115 \text{ mm}$:

$$G_{IIc} = \frac{P_c^2}{2BW} \frac{dC}{d(a/W)}. \quad (1)$$

2.2. Coating characterization

Representative as-sprayed cross-sections and coating surfaces from each batch were examined using optical and scanning electron microscopy respectively. A system, termed Quality Indices, was devised to quantify those microstructural features that were expected to reduce the coating toughness of these coatings and were

amenable to inspection. Each batch was ranked in terms of a Cross-sectional Quality Index and a Surface Quality Index. The indices were assigned in accordance with the priorities shown in Table 1 and ranged from 1, the 'worst' of the nine batches, to 9, the 'best'. A subjective judgement was made regarding the severity of each feature and the consequent ranking of that coating. For example if a coating had a very high macroporosity, it received a worse ranking than a coating containing relatively few unmelted particles, despite the higher priority of the unmelted particles.

3. Results

3.1. Quality indices

The Cross-sectional and Surface Quality Indices are shown, with a description of the coatings, in Tables 2 and 3 respectively. Micrographs of coatings from these batches, arranged in descending order of their Quality Indices, are shown in Figs. 3 and 4.

3.2. Fracture toughness

A plot of coating toughness for batches 1–8 is shown in Fig. 5. The compliance data for batch 9 were erratic due to slipping of the loading fixtures on the substrates and adherends, and therefore no compliance calibration curve or toughness calculations were made for this batch.

3.3. Fractography

3.3.1. APS NiAl

Unfortunately, all but two of the specimens from batches 1 and 2 failed at the epoxy–coating or epoxy–adherend interface. Clearly, the toughness of the coating

exceeded that of the adhesive and therefore the data shown in Fig. 5 for these batches must be regarded as a lower bound. In the two specimens where the fracture path was located entirely within the coating, cohesive failure, the fracture surfaces were reasonably rough and contained many shear hackles, a characteristic feature of mode II failure surfaces in polymer matrix composites [24].

The shear hackles in these coatings consisted of individual, or small groups of, lamellae partially separated and lifted from the body of the coating, a typical example being shown in Fig. 6(a). Shear hackles have not been previously reported on thermal spray coatings, although it is likely that the features termed 'fish scales', observed on the fracture surface of shear test specimens [25], were hackles. This suggested that very high levels of mode II loading, which produced the hackles in these specimens, are not present in service.

On one of the specimens that had failed cohesively, ten to twenty 1 mm x 1 mm regions had been abraded, as shown in Fig. 6(b). Similar marks were found in the corresponding positions on the adherend side of the crack. The opposing crack faces had remained in contact following failure, and continued specimen displacements caused micro-machining of the contracting asperities. Such features are an artefact of continued mode II displacements and are not expected to be representative of service failures, where crack faces are free to separate.

3.3.2. APS NiAl then Al₂O₃

All specimens from these batches exhibited similar failure features. The first 1–20 mm ahead of the notch root failed at the epoxy–adherend interface. Subsequent propagation occurred cohesively within the coating, either wholly within the ceramic (batches 3–5), or at the bond coat–ceramic interface (batch 6). The failure surface in batches 3–5 was quite smooth, as shown in Fig. 7. Almost the entire failed surface area consisted of micropores. Dispersed through these were regions of well-bonded lamellae that had fractured during the test. As with the APS NiAl coatings, these fracture surfaces contained fine shear hackles.

3.3.3. APS NiAl then YSZ

All specimens from batch 8 and eight specimens from batch 7 failed cohesively within the YSZ, a typical fracture surface being shown in Fig. 8(a). In the remaining four specimens from batch 7, the first 20–40 mm of failure were cohesive in the ceramic, followed by failure at the bond coat–ceramic interface. A representative fractograph of the interfacial fracture is shown in Fig. 8(b).

3.3.4. LPPS TiNi

All specimens failed within the glue-line, either at the coating–epoxy interface or at the epoxy–adherend inter-

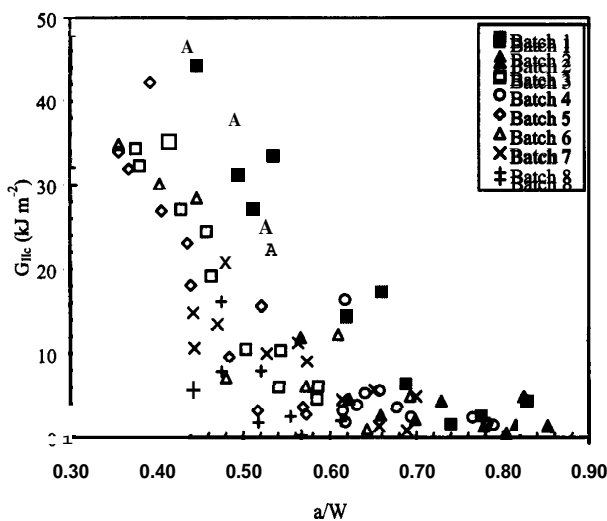


Fig. 5. Toughness of APS coatings for batches 1–8.

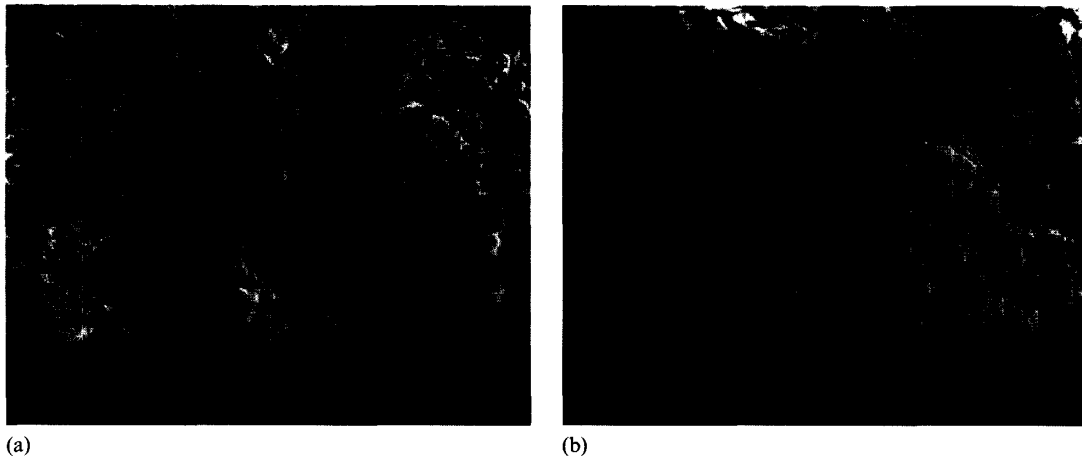


Fig. 6. (a) Cohesive failure from batch 1. The region immediately above the horizontal crack is raised from the bulk coating. (b) Abrasion marks as observed on small regions of the fracture surface shown in (a).

face. In no instance did a LPPS TiNi coating fail, and thus, no indication of the mode II failure morphology was obtained.

4. Discussion

4.1. Fracture toughness

The G_{IIc} of all coatings decreased as the crack length increased until, for crack lengths beyond $a/W=0.70$, the coatings failed at almost constant G_{IIc} . This trend is typical for materials containing large process zones, such as concrete, where the crack must reach a substantial length before failure can be predicted using linear elastic fracture mechanics [26]. The change in toughness with crack length has been observed for the G_{Ic} of thermal spray coatings in double cantilever beam tests [19]. This effect was thought to be due to changes in the mode of bending in the specimen as the crack propagated, but a comprehensive explanation has yet to be presented.



Fig. 7. Typical cohesive failure surface representative of batches 3–5.

The G_{Ic} values of APS NiAl, Al_2O_3 and YSZ coatings have been reported as 350 [27], 12–27 [27] and 33–56 [28] $J m^{-2}$, respectively. Corresponding values of G_{IIc} from these tests, for $a/W>0.7$, were 2300, 3200 and 2800 $J m^{-2}$, a rise of one to two orders of magnitude. In monolithic materials, the mode I and mode II fracture toughness tends to lie within a factor of two [29–31], although rises of an order of magnitude [32,33] or greater [34] have been reported. These differences are generally attributed to some microstructural feature such as the additional load required to produce mode II displacement of crack faces in material structures which contain interlocking grains [30]. It is likely that the highly directional microporosity in thermal spray coatings causes the larger difference between G_{IIc} and G_{Ic} , although further work is required to determine the mechanism for this increase.

4.2. Failure mechanism

Examination of the fracture surfaces of thermal spray coatings, from both the mode II tests performed in this work and the mode I tests reported in the literature, reveal that a large proportion of failure surfaces are quite smooth and unlike the appearance of traditional fracture surfaces. There are no dimples characteristic of ductile rupture or river patterns signifying brittle fracture. In general, there is no evidence of mode I cracking parallel to the surface of lamellae. There are, however, many fresh fracture surfaces in the form of trans-lamellar cracks. It is proposed that the smooth surfaces are the faces of micropores and that failure occurs as a result of the propagation of discrete trans-lamellar microcracks between neighbouring micropores. As shown in Fig. 9, each trans-lamellar microcrack connects two existing micropores, and thus facilitates substantially faster crack growth that would be predicted by considering only the surface area of fresh cracking.

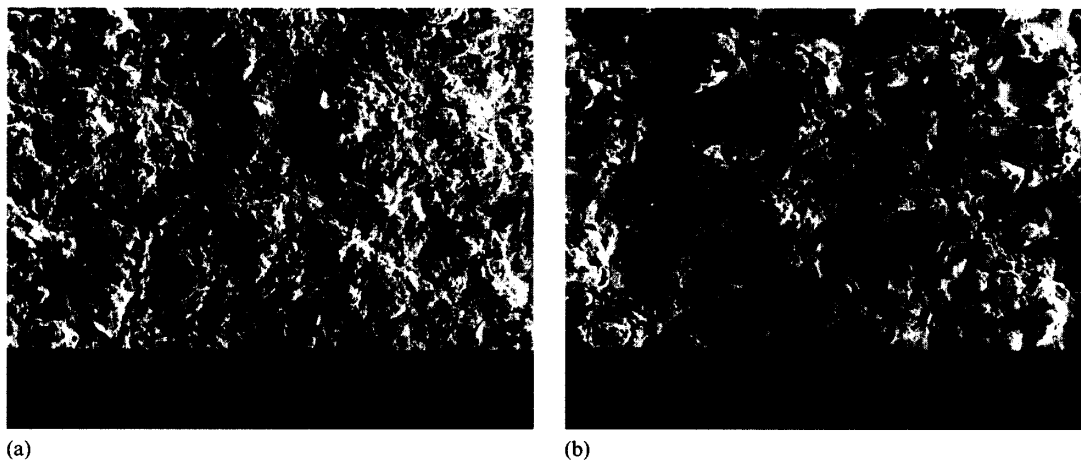


Fig. 8. (a) Representative cohesive failure surface for APS YSZ. (b) Representative failure surface at the bond coat–ceramic interface for four of the batch 7 specimens.

Failure occurs when sufficient micropores have been connected by trans-lamellar microcracks to separate that region from the remainder of the coating.

Two of the unique microstructural features of thermal spray coatings facilitate this mechanism. Firstly, the majority of the fracture surface pre-exists in the as-sprayed coating as micropores. The only fresh crackling required is that to link these surfaces together. Secondly, this microporosity is oriented approximately in the plane of the coating. Therefore, most microcracks, which are simply micropores connected by trans-lamellar microcracks, also tend to be oriented in this plane. This results in spalling, which is particularly detrimental to

coating performance and is the type of failure that is observed in service.

Paradoxically, while microporosity is responsible for the low fracture toughness of thermal spray coatings relative to the monolithic material, it is also the reason for their excellent operational performance. The propagation of trans-lamellar microcracks and linking of micropores effectively relieves local stresses, leaving the bulk of the coating relatively unaffected. Local stresses induced by thermal shock, thermal cycling, mechanical loading of the substrate, oxidation and corrosion products, can therefore be accommodated. In contrast, if the coating were monolithic and contained no microcracks, these stresses would be transmitted through the entire coating and result in massive coating fracture. This suggests that there is an optimal specific area fraction of true interlamellar contact. This area fraction would be sufficiently high to maximize the density of microcracks required to produce coating failure, but not so high that applied stresses would be transmitted throughout the entire coating.

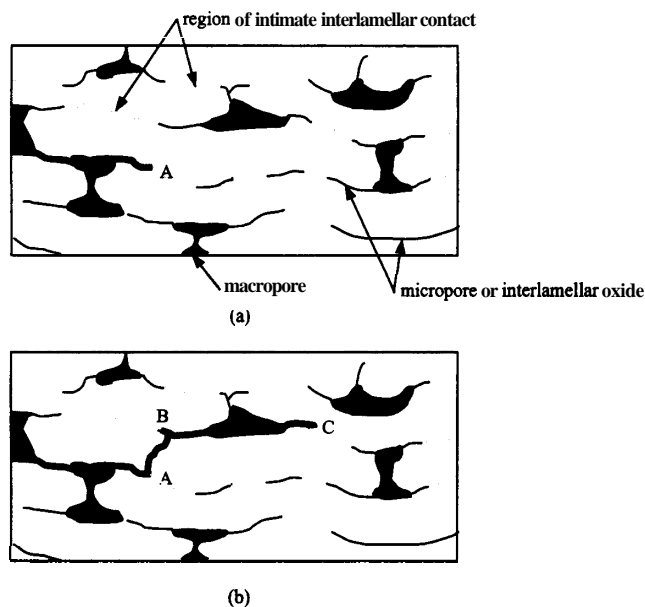


Fig. 9. Schematic representation of the crack propagation mechanisms within thermal spray coatings. (a) The original configuration, with the tip of a macro-crack at position A. (b) The propagation of a short trans-lamellar microcrack, from Position A to B, will result in an effective extension of the macro-crack to Position C.

4.3. Quality indices

The Cross-sectional and Surface Quality Indices were used to rank the coatings in terms of those microstructural features considered most important in the control of the coating toughness. The indices used in this work were subjective and not taken from a standard or absolute scale. Commercial thermal spray operators have internal standards to rate the quality of coatings, one system being to compare the coating under examination with a series of micrographs showing coatings ranging in quality from 'good' to 'bad'. It is not possible to develop an absolute rating at present because the effect of the most important variables controlling coating toughness, (1) the fraction of interlamellar area in intimate contact, (2) the geometry and distribution of

microcracks, (3) the number and volume of unmelted particles, and (4) the volume fraction and distribution of macroporosity, have not been quantified. This requires substantial research. Once the effects of these microstructural features are understood and an absolute characterization system developed, then the system of Quality Indices should be amenable to automation using image analysis techniques.

4.4. Relation between fracture toughness and microstructure

4.4.1. General

If the proposal made earlier in this paper were correct, then G_{IIC} should be a function of coating quality, regardless of the coating material. To test this hypothesis, a least-squares quadratic fit was made through the Fig. 5 data for each material. These regression curves were then solved for G_{IIC} at $a/W=0.4, 0.5, 0.6$ and 0.7 . Also, the Surface Quality Index and Cross-sectional Quality Index, for each batch, were summed to produce a Combined Quality Index. In Fig. 10 the resultant values of G_{IIC} were plotted against the Combined Quality Index. The Combined Index was used to simplify the analysis, by reducing two Indices to a single value for each batch. Generation of the Combined Index by assuming each Index to have an equal weighting was considered a reasonable first approximation since the Surface and Cross-sectional indices are complimentary, a reduction in the severity of defects in the cross-sections of coatings (increase in Cross-sectional Quality Index) should be associated with a corresponding increase in the degree of particle melting (increased Surface Quality Index).

Three features are evident in Fig. 10. Firstly, as discussed previously, toughness decreased as a/W increased. Secondly, for each crack length, the toughness

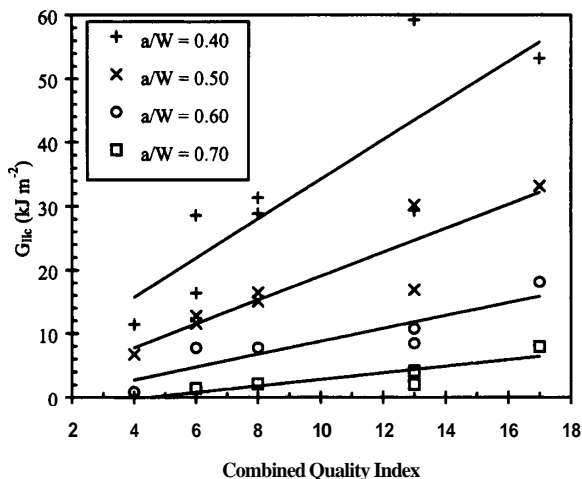


Fig. 10. Plot of fracture toughness versus the Combined Quality Index (sum of the Cross-sectional and Surface Quality Indices) for the indicated crack lengths.

increased as the Combined Quality Index increased. This is significant since it verifies that the Indices were indeed identifying those features that controlled the fracture toughness of these coatings. The coatings with greater numbers of microcracks parallel to the substrate, unmelted particles and larger macroporosity exhibited a lower G_{IIC} . Finally, as a/W increased, the slope of the G_{IIC} versus Combined Index lines decreased. Further work will be required to determine whether this decreased discrimination between coatings at longer crack lengths was caused by a genuine coating response or specimen geometry effects.

4.4.2. APS NiAl

The quality of the APS NiAl coatings was good, which is reflected in their high Quality Indices. The feature detracting from the quality of these coatings was a thin layer of oxide surrounded most lamellae (Fig. 3). It is very difficult to eliminate this feature when spraying metallic materials in air. It has been reported that the effect of oxidation on the strength of NiAl coatings is lower than for most other metals because the exothermic oxidation of Al releases sufficient heat to delay the solidification of the freshly impacted droplet. This extends the time at the elevated temperature and increases the probability of bonding between the lamellae.

For $a/W < 0.6$, the toughness of NiAl coatings was more than double that of the duplex coatings. Surprisingly, the steady-state values were inferior to those of other coatings. For $a/W > 0.7$, the G_{IIC} of NiAl, NiAl + Al_2O_3 and NiAl + YSZ were 2.3, 3.2 and 2.8 kJ m^{-2} , respectively. Certainly, the NiAl data were considered a lower bound since failure occurred within the adhesive between the coating and adherend. It is likely that the actual G_{IIC} of NiAl is double or triple that obtained in these tests. However, even at this level, it is still of the same order as that of the duplex coatings. This appears anomalous, the toughnesses of metals are typically one to two orders of magnitude greater than that of ceramics. It is proposed that this similarity is caused by the high number of atomically sharp micro-pores oriented parallel to the plane of the coating. These defects permit each propagation of the trans-lamellar microcracks that cause coating failure. Thus, although the intrinsic toughness of the coating material is important, it is the microstructure that dictates coating toughness.

4.4.3. APS NiAl then Al_2O_3

The qualities of the APS NiAl + Al_2O_3 coatings were rather erratic, indicating large variations that may be obtained in a coating microstructure under even nominally identical spray conditions. For example, coatings from batch 5 contained low-porosity, large cracks perpendicular to the plane of the coating and poor surface

melting, whereas coatings from batch 6, which were deposited under nominally identical conditions, were highly porous and reasonably well melted. Clearly, very close control of the spray equipment is required to eliminate these variations and maintain a consistent coating quality.

Some of the defects observed in these coatings could be attributed to changes in deposition parameters. It is most likely that the band of microcracks parallel to the plane of the coating in batch 4 was caused by an interruption during spraying. This batch was deposited in two sets of four passes, with a 15-min break between each set to allow the substrate to cool. The differential thermal contraction between the cooled substrate and the remainder of the coating generated sufficient residual stresses to cause parallel cracking. However, this effect was not observed in batch 3, which was also deposited in two sets of passes. In batch 3, the raster distance (the lateral separation between successive passes of the plasma torch over any particular point on the coating was increased), which reduced the extent of local thermal excursions and allowed the thermal energy in the freshly deposited coating to be conducted into the substrate, thereby reducing thermal gradients and the tendency for parallel microcracking.

4.4.4. APS NiAl then YSZ

In batches 7 and 8 severe cracks were observed parallel and perpendicular to the coating surface. As with batch 4 these cracks were caused by overheating of the coating, as a result of the raster distance and traverse speed being too low. In addition the melting of particles by the plasma plume during depositions were incomplete, resulting in the rough coating surface and lack of through-lamellae microcracks. To improve melting, the spray distance or powder feed rate should be decreased and/or the torch power increased.

4.4.5. LPPS TiNi

The TiNi coatings appeared almost fully dense, despite significant numbers of unmelted particles. In an APS system, such particles would be expected to significantly reduce the toughness of the coating. However, the insert atmosphere within the LPPS chamber prevented oxidation of the liquid droplets and freshly deposited lamellae, permitting subsequent layers to wet these surface and produce substantial area fractions of intimate contact. Therefore, the presence of the unmelted particles within the coating was expected to have a less significant effect than an equivalent APS coating. This was supported by the fracture toughness results where the epoxy adhesive failed before any damage was inflicted on the TiNi coatings.

In these specimens, the toughness of the coating had exceeded that of the adhesive. The mode II specimen, which was constructed by bonding a coated substrate

to an adherend, can only generate valid data when the adhesive is tougher than the coating. This is readily achievable for most thermal spray coatings, including ceramics and many flame-sprayed metals, using existing epoxy adhesives. However, as demonstrated in this batch, this is not the case for high toughness coatings. Such coatings are becoming more common through improved control over existing thermal spray processes and modern deposition techniques. These situations will demand either adhesives with higher toughness or alternative test specimen geometries that do not rely on bonded adherends.

4.5. Failure map

The Quality Indices, fracture surface observations and G_{IIc} data were used to produce the failure map shown in Fig. 11. To construct this map, each batch was plotted according to its Cross-sectional and Surface Quality Indices. The failure morphologies of these batches were then used to generate the three characteristic failure zones. Finally, the G_{IIc} , determined using the data from Fig. 10 at $a/W=0.70$, were plotted onto the map as a family of diagonal lines (noting that the Combined Index was the sum of the Cross-sectional and Surface Quality Indices).

In general, the Surface Quality Indices matched the Cross-sectional Indices, and so the batches were clustered along the 45° diagonal of the map. This was expected, and supported the selection of the Combined Quality Index as the sum of the individual Quality Indices. The particular circumstances of the two batches

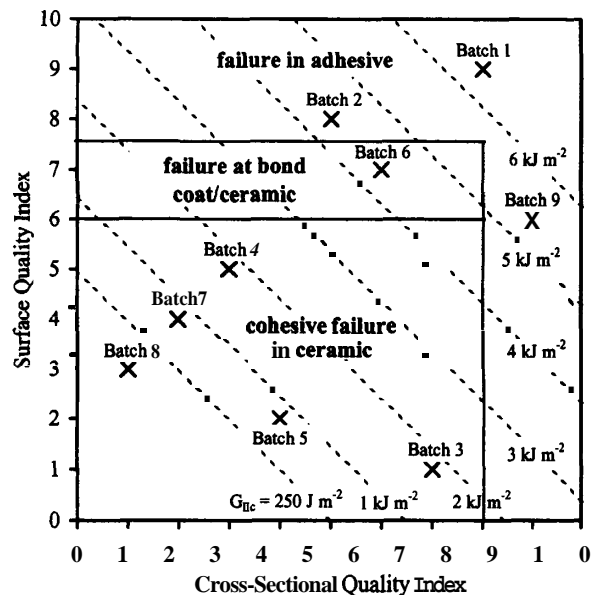


Fig. 11. Failure map for the thermal spray coatings tested in this work. The dashed diagonals are lines of constant G_{IIc} , the value of which is shown at the right-hand end of each diagonal. These data are derived from the $a/W=0.7$ line in Fig. 10.

that did not follow this trend, batches 3 and 9, have been discussed previously.

The toughness increased as the failure morphology changed from cohesive within the ceramic, to the bond coat/ceramic interface, to the adhesive. Most duplex coatings failed cohesively within the ceramic, although the highest quality of these coatings failed at the bond coat–ceramic interface. It appears that to maximize the performance of duplex coatings, it is necessary to ensure that the ceramic is sufficiently well bonded that it is the interface with other materials, such as the metallic bond coat, which becomes the weak link. Techniques have been developed to minimize property changes through coatings and thus increase the energy required to generate interfacial failure. These include the use of feedstock, which contains both ceramic and metallic powders, or grading the coating by increasing the proportion of ceramic in the feedstock as spraying proceeds.

5. Conclusions

A novel test specimen geometry has been developed to determine the mode II fracture toughness, G_{IIc} , of thermal spray coatings. The data generated by this test will complement those obtained from existing mode I tests, since operational coatings are subjected to both mode I and mode II loading. Nine batches of APS NiAl, APS NiAl+Al₂O₃, APS NiAl+YSZ and LPSS TiNi coatings were tested using the mode II specimen. The apparent G_{IIc} for each coating decreased as crack length increased until, for cracks beyond $a/W \approx 0.70$, it was approximately constant in the range of 2.3–3.2 kJ m⁻². This is one to two orders of magnitude greater than the G_{Ic} of similar coatings.

It was proposed that the microstructure of thermal spray coatings controls their toughness. Therefore, the concept of Cross-sectional and Surface Quality Indices was introduced, where coatings were ranked in terms of the severity of those microstructural features considered to be both important to the failure process and amenable to inspection. A failure map was developed to display the relations between the Quality Indices, failure morphology and G_{IIc} of these coatings. It showed that as the Quality Indices rose, regardless of the coating material, then a commensurate rise was observed in toughness. In addition, the failure morphology changed from cohesive within the ceramic to failure at the bond–coat ceramic interface. The Quality Indices and failure map show considerable potential as instruments to quantitatively assess the effect of individual microstructural features on coating toughness.

Acknowledgements

This work was performed in the Department of Materials Engineering, Monash University (Melbourne,

Australia) under support from the Australia Research Council. The authors acknowledge the assistance that was provided by the Departmental technical staff. The contribution of Associate Professor J. Griffiths through many detailed conversations is also gratefully appreciated.

C. Berndt acknowledges the support from the National Science Foundation (NSF) under the MRSEC Program DMR 9632570.

Acknowledgement is given to the CSIRO — Division of Manufacturing Technology for providing access to their plasma spray facilities at their Woodville North Site. The LPPS coatings were deposited at the Guangzhou Research Institute of Non-Ferrous Metals, China. The authors acknowledge the Australian Ministry of Industry and Technology in funding this part of the work.

References

- [1] T.A. Taylor, D.L. Appleby, A.E. Weatherill, J. Griffiths, *Surf. Coat. Technol.* 43/44 (1990) 470.
- [2] H.D. Steffens, U. Fisher, *Nat. Therm. Spray. Conf. Cincinnati, OH* (1988) 167.
- [3] K.-S. Shi, Z.-Y. Qian, M.-S. Zhuang, *J. Am. Ceram. Soc.* 71 (1988) 924.
- [4] Y. Arata, A. Ohmari, C.-J. Li, *Proc. Int. Symp. Adv. Therm. Spray Tech. and Allied Coat.*, Osaka, Japan (1988) 205.
- [5] R. McPherson, P. Cheang, *12th Int. Therm. Spray Conf.*, London, (1989) Paper 17.
- [6] S. Kuroda, T.W. Clyne, *Thin Solid Films* 200 (1991) 49.
- [7] S.C. Gill, *Ph.D. thesis*, Gonville and Caius College, Cambridge, UK, 1991.
- [8] G. Johner, V. Wilms, K.K. Schweitzer, *ASME Paper* 88-GT-313, (1988)
- [9] S. Sturlese, R. Dal Maschio, C. Bartuli, N. Zacchetti, M. Bernardi, *7th CIMTEC World Ceramics Congress*, Montecatini, Terme, Italy, (1990) Paper S1.2A-LO8.
- [10] T.E. Strangman, *Thermal Barrier Coat Workshop*, NASA Lewis Research Center, Cleveland, OH (1985) 1.
- [11] R. McPherson, *Thin Solid Films* 83 (1981) 297.
- [12] G.C. Chang, W. Pucharoen, R.A. Miller, *Surf. Coat. Technol.* 30 (1987) 13.
- [13] R. Elsing, O. Knotek, U. Balting, *Surf. Coat. Technol.* 43/44 (1990) 416.
- [14] R.A. Miller, *ASME J. Eng. Gas Turbines and Power* 111 (1989) 301.
- [15] H. Djabella, R.D. Arnell, *Thin Solid Films* 223 (1993) 87.
- [16] M.J. Filiaggi, R.M. Pilliar, *J. Mater. Sci.* 26 (1991) 5383.
- [17] S.J. Howard, T.W. Clyne, *Surf. Coat. Technol.* 45 (1991) 333.
- [18] F. Beltzung, G. Zambelli, E. Lopez, A.R. Nicoll, *Thin Solid Films* 181 (1989) 407.
- [19] C.C. Berndt, *Ph.D. thesis*, Monash University, Victoria, Australia, 1980.
- [20] P.J. Callus, C.C. Berndt, *Int. J. Fract.* 43 (4) (1990) R57.
- [21] P.J. Callus, C.C. Berndt, *7th CIMTEC World Ceramics Congress*, Montecatini, Terme, Italy, (1990) Paper S1.2A-LO3.
- [22] P.J. Callus, *Ph.D. thesis*, Monash University, Victoria, Australia, 1993.
- [23] B.R. Lawn, T.R. Wilshaw, *Fracture of Brittle Solids* Cambridge

Solid State Science **Series** Cambridge University Press, London, 1975.

[24] G.E. Morris, ASTM STP 969, Philadelphia, PA (1979) 274.

[25] T.A. Cruse, R.C. Dommarco, P.C. **Bastias**, *ASME J. Eng. Mater. Tech.* 120 (1998) 26.

[26] K. Visalvanich, A.E. Naaman, ASTM STP 745, Philadelphia, PA (1981) 141.

[27] P. **Ostojic**, R. **McPherson**, *Mater. Sci. Forum* 34–36 (1988) 451.

[28] D.Z. Guo, L.J. Wang, *Surf. Coat. Technol.* 56 (1992) 19.

[29] D.L. Jones, D.B. Chisholm, *Eng. Fract. Mech.* 7 (1975) 261.

[30] D. Singh, D.K. Shetty, *ASME Paper* 88-GT-208, (1988)

[31] M. Yoda, *Proc. Int. Conf. AUSTCERAM 92 Vol. 2* (1992) 957.

[32] S. Mall, N.K. Kochlar, *Eng. Fract. Mech.* 31 (5) (1988) 747.

[33] H. Chai, *Int. J. Fract.* 37 (1988) 137.

[34] S.A. Hamoush, S.H. **Ahmad**, *Int. J. Adhesion Adhesives* 9 (3) (1989) 171.